2018-04-20

Effects of ion magnetization on the Farley-Buneman instability in the solar chromosphe

Draft version March 9, 2018
Preprint typeset using LaTeX style AASTeX6 v. 1.0

EFFECTS OF ION MAGNETIZATION ON THE FARLEY-BUNEMAN INSTABILITY IN THE SOLAR CHROMOSPHERE

Alex C. Fletcher, Yakov S. Dimant, Meers M. Oppenheim
Center for Space Physics
Boston University
725 Commonwealth Ave., Boston, MA 02215

Juan M. Fontenla
NorthWest Research Associates
3380 Mitchell Lane, Boulder, CO 80301

ABSTRACT

Intense heating in the quiet-Sun chromosphere raises the temperature from 4000 K to 6500 K but, despite decades of study, the underlying mechanism remains a mystery. This study continues to explore the possibility that the Farley-Buneman instability contributes to chromospheric heating. This instability occurs in weakly ionized collisional plasmas in which electrons are magnetized but ions are not. A mixture of metal ions generate the plasma density in the coolest parts of the chromosphere; while some ions are weakly magnetized, others are demagnetized by neutral collisions. This paper incorporates the effects of multiple, arbitrarily magnetized species of ions to the theory of the Farley-Buneman instability and examines the ramifications on instability in the chromosphere. The inclusion of magnetized ions introduces new restrictions on the regions in which the instability can occur in the chromosphere - in fact it confines the instability to the regions in which heating is observed. For a magnetic field of 30 G, the minimum ambient electric field capable of driving the instability is 13.5 V/m at the temperature minimum.

1. INTRODUCTION

Semi-empirical models of the quiet-Sun chromosphere show a temperature minimum of $\sim$4000 K followed by a steep increase of $\sim$2500 K to a plateau (Fontenla et. al. 1991, 1993). While the responsible mechanism is unknown, a temperature plateau of 6000-7000 K is necessary to explain UV continuum and line emissions (Athay, R. G. 1966). Researchers have proposed a number of physical mechanisms, including transient shock wave heating, nano-flares associated with magnetic reconnection, Joule heating due to continuous dissipation of MHD waves, and anomalous heating associated with plasma turbulence (Fontenla et. al. 2009).

Carlsson, M. and Stein, R. F. (1992) performed self-consistent radiation hydrodynamic simulations that showed shocks are formed due to convective motions of neutral particles from the upper photosphere. There is enough energy in this neutral flow to explain chromospheric heating, but the shocks would inhibit emissions during the shock expansion phase, and this has not been observed (Carlsson, M. 2007). The expected Pederson and parallel conductivities in the chromosphere suggest a relatively low rate of Joule heating; insufficient to explain the electron temperature increase (Fontenla et. al. 2008). Anomalous electron heating is associated with the Farley-Buneman instability (FBI) in the ionosphere (Oppenheim and Dimant 2013, and references therein), and in the chromosphere heating in this manner would be consistent with the measured spectra and as well as the correlation of the UV intensity distribution with magnetic fields (Fontenla et. al 2007).

Farley, D. T. (1963) and Buneman, O. (1963) first described the FBI as a modified two-stream instability in which the relative electron-ion drift speed exceeds the ion acoustic velocity. This causes density irregularities in the equatorial and auroral ionosphere. In the auroral ionosphere it causes intense electron heating, raising the electron temperature by as much as 10 fold (Foster and Erickson 2000; Bahcivan, H. 2007). In the simplest case, the ions move with the neutrals due to collisions but electrons, which unlike the ions are magnetized, move according to the $\mathbf{E} \times \mathbf{B}$ (Hall) drift. The FBI is traditionally studied in the context of the ionosphere, but the conditions for the instability also exist

in the chromosphere (Fontenla 2005; Gogoberidze et. al. 2009; Madsen et. al. 2014; Gogoberidze et. al. 2014).

The low temperatures in the chromosphere mean that most of the H is neutral but some plasma exists, dominated by protons (H^+) and heavy metals such as silicon (Si^+), magnesium (Mg^+), and iron (Fe^+). Near the temperature minimum, H^+ is weakly magnetized (depending on the magnetic field, of course) while the metals are collisionally demagnetized. The metals are the dominant ions in the lower chromosphere while the protons are the dominant ions in the upper chromosphere. It is also no longer convenient to think in terms of a critical drift velocity since there are many drift velocities that come into play (the Hall and Pederson drift for each species, though electrons are distinct and the main driver of the instability). Instead, we consider a critical ambient electric field that is responsible, along with the magnetic field, for these drifts. The considered electric field is in the local frame of the neutral flow. We can then recover a trigger speed by dividing the threshold field by the ambient magnetic field, B.

A neutral dynamo (Dimant et. al. 2016) associated with convective motions from the photosphere (Fontenla et. al. 2008) could produce the background electric field. Gogoberidze et. al. (2009), Fontenla (2005), Gogoberidze et. al. (2014), and Fontenla et. al. (2008) employed a theory with a single ion species that is more appropriate for the ionosphere. Madsen et. al. (2014) expanded this theory to include multiple unmagnetized ion species. In this paper, we include multiple arbitrarily magnetized ion species and analyze how this new factor affects the possible heating of the chromosphere due to the FBI.

The paper is laid out as follows. Section 2 reviews a model of the chromosphere. Section 3 presents a dispersion relation for the instability with multiple magnetized ion species. A derivation of a phase velocity relation, growth/damping rate, and threshold electric field for three cases follows. Section 4 describes the numerical approach to solving the dispersion relation and finding the threshold field. In Section 5, we find the threshold field and trigger speed given conditions found in the temperature minimum region of the chromosphere and discuss the differences caused by allowing the ions to be magnetized.

2. MODEL OF THE SOLAR CHROMOSPHERE

In order to calculate the threshold field for instability in the chromosphere, we need to know the species-neutral collision frequencies, which require the number densities of the neutrals and plasma species as well as temperatures as functions of altitude. We use the Fontenla et. al. (2009) quiet-Sun chromosphere model to obtain these values.

Figure 1 shows the electron temperature provided by the model. The temperature minimum is at ~800 km and the heating region directly above it. The temperature minimum is designated in the figures with the dashed horizontal line.

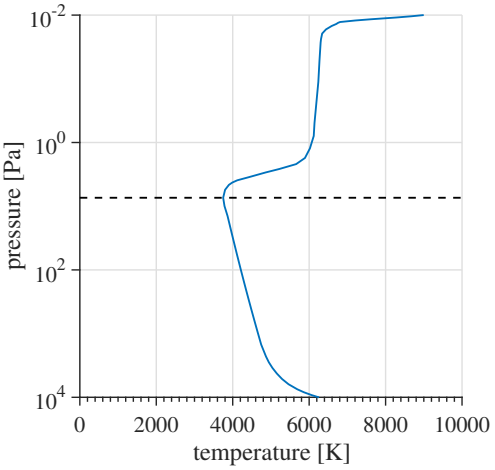

Figure 1. The electron temperature in the chromosphere. The dashed line denotes the altitude of the temperature minimum while the heating region is seen between 800 and 1000 km.

Figure 2 shows the number density of the neutral hydrogen and the ions we have included in the analysis. We chose to include H^+ as well as the dominate metals mentioned in Section 1 (Mg^+, Si^+, and Fe^+). We also include carbon (C^+) because there may be layers in which it is important. At nearly every altitude, the density of neutral hydrogen is orders of magnitude higher than that of the charged species, consistent with the plasma being weakly ionized. The

rapid changes at ∼1900 km indicate the imminent transition to the corona.

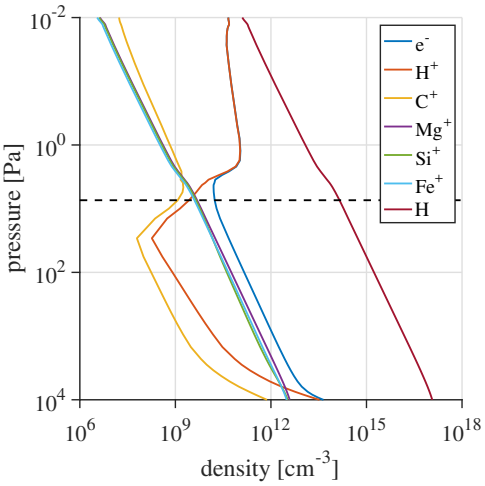

Figure 2. The number densities of electrons, hydrogen ions (protons), carbon ions, magnesium ions, silicon ions, iron ions, and hydrogen neutrals in the chromosphere. The horizontal dash line represents the temperature minimum.

We consider three types of collisions: momentum transfer, resonant charge exchange between H and H^+, and Coulomb collisions between electrons and ions (but not intraspecies Coulomb collisions). The collision frequency used in the dispersion relation in the following section is approximated as the sum of these three collision frequencies. A classical model of collisions between any charged species and neutrals is provided by Dalgarno et. al. (1958),

$$\nu_{sn} = 2.21\pi n_n \sqrt{\frac{\alpha_n e^2}{4\pi\epsilon_0 \mu_{sn}}}, \tag{1}$$

where n_n is the neutral number density, α_n is the polarizability, μ_{sn} is the reduced mass, ϵ_0 is the vacuum permittivity, and s denotes the species. Schunk and Nagy (2009) provide a resonant charge exchange collision frequency of

$$\nu_{res} = 2.65 \cdot 10^{-16} n_H \sqrt{T_{H^*}} \left(1 - 0.083 \log_{10} T_{H^*}\right)^2, \tag{2}$$

where n_H is the number density of neutral hydrogen (in m^{-3}) and T_{H^*} is the average temperature of H and H^+ (in K). For Coulomb collisions, the collisions frequency with the Spitzer correction is

$$\nu_{je} = \frac{\pi n_e e^4 \ln(12\pi n_e \lambda_D)}{(4\pi\epsilon_0)^2 \sqrt{m_s (2k_b T)^3}}, \tag{3}$$

where the Debye length, λ_D, is given by

$$\lambda_D = \sqrt{\frac{\epsilon_0/e^2}{n_e/k_b T_e + \sum_j Z_j^2 n_j / k_b T_j}}, \tag{4}$$

where Z_j is the charge state of the j^{th} ion. Madsen et. al. (2014) provides a discussion of the accuracy of these frequencies. The ratio of cyclotron frequency to the sum of these collision frequencies is shown in Figure 3. At the temperature minimum and heating regions, it can be seen that the electrons are magnetized, the metals are demagnetized, and the protons are somewhere in the middle.

The mean drift velocities are given by a combination of the Pedersen and Hall drifts,

$$\mathbf{u}_{s0} = \frac{\kappa_s(\kappa_s \mathbf{E} \times \mathbf{b} + \mathbf{E})}{(1 + \kappa_s^2) B}, \tag{5}$$

and the corresponding speeds are shown in Figure 4. In Equation (5), $\kappa_s = \Omega_{cs}/\nu_s$ is the magnetization and $\Omega_{cs} = q_s B/m_s$ is the gyrofrequency. At the temperature minimum, the proton drift speed is about one quarter the electron drift speed and κ_{H^+} is 0.1-1, meaning proton magnetization certainly cannot be neglected.

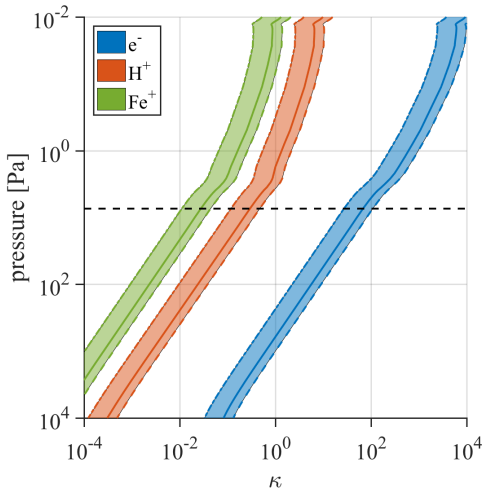

Figure 3. The ratio of gyrofrequency to collision frequency, $\kappa = \Omega_c/\nu_n$, for electrons, protons, and iron (the heaviest ion under consideration). The shaded regions represent the κ between 20 G (left, dash-dot) and 80 G (right, dash). The solid line is the κ for a magnetic field of 50 G. The horizontal dash line represents the temperature minimum.

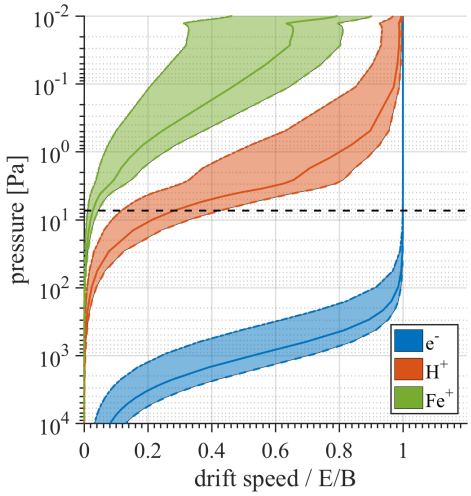

Figure 4. The drift speed, Equation 5, normalized to the $\mathbf{E} \times \mathbf{B}$ speed for magnetic fields between 20 G (dash-dot) and 80 G (dash). The solid line is for a magnetic field of 50 G. The horizontal dash line represents the temperature minimum.

3. FARLEY-BUNEMAN INSTABILITY THEORY

This section contains a dispersion relation, growth rate, and threshold electric field for the FBI that includes arbitrarily magnetized ions and strongly magnetized electrons.

3.1. *Dispersion Relation*

Our treatment is based on the multi-fluid plasma equations in the local neutral frame of reference. In the simplest form, these equations include the momentum equations for inertialess electrons (e) and each of the single-charged ion species (j),

$$0 = -e\mathbf{E}_0 + e\nabla\phi - e(\mathbf{u}_e \times \mathbf{B}) - \frac{\nabla(n_e T_e)}{n_e} - m_e \nu_e \mathbf{u}_e, \tag{6a}$$

$$m_j \frac{D\mathbf{u}_j}{Dt} = e\mathbf{E}_0 - e\nabla\phi + e(\mathbf{u}_j \times \mathbf{B}) - \frac{\nabla(n_j T_j)}{n_j} - m_j \nu_j \mathbf{u}_j, \tag{6b}$$

along with the corresponding continuity equations,

$$\frac{\partial n_e}{\partial t} + \nabla \cdot (n_e \mathbf{u}_e) = 0, \qquad \frac{\partial n_j}{\partial t} + \nabla \cdot (n_j \mathbf{u}_j) = 0. \tag{7}$$

Here $D/Dt \equiv \partial/\partial t + \mathbf{u}_j \cdot \nabla$ is the material derivative and t is time; n is the number density, $\mathbf{u}$ is the fluid velocity, T is the temperature (in energy units), ϕ is the electrostatic potential, ν is the collision frequency, e is the elementary charge, and m is the mass; and $\mathbf{E}_0$ and $\mathbf{B}$ are the external electric and magnetic fields in the local neutral frame. For wave processes caused by small-scale instability, we assume homogeneous and constant local average fields and fluid characteristics. Equations (6) and (7) neglect collisions between the charged particles (relative to their collisions with neutrals), gravity, as well as ionization, recombination, and charge exchange. We also neglect perturbations of the magnetic field and temperatures, and assume local quasi-neutrality, $n_e = \sum_j n_j$.

Bearing in mind small wave perturbations, we consider solutions of Equations (6) and (7) of the form

$$A = A_0 + \hat{A}, \qquad \hat{A} = \sum_{\omega,\mathbf{k}} \delta A(\omega, \mathbf{k}) \exp(-i\omega t + i\mathbf{k} \cdot \mathbf{x}), \tag{8}$$

where A_0 is the equilibrium quantity, $\hat{A}$ is the corresponding perturbation with the complex wave amplitude δA, $\mathbf{k}$ is the real wave vector, and $\omega = \omega_r + i\gamma$ is the complex wave frequency. In this ansatz, instability requires the positive growth rate, γ. In the linear theory with $|\delta A| \ll A_0$, the complex wave frequency becomes a function of $\mathbf{k}$ through the dispersion relation that we obtain below.

The linearized momentum equations corresponding to Equation (6) are

$$\delta \mathbf{u}_e = \mathbf{G}_e \left(\delta\phi - \frac{T_e}{e} \frac{\delta n_e}{n_{e0}} \right), \qquad \delta \mathbf{u}_j = \mathbf{G}_j \left(\delta\phi + \frac{T_j}{e} \frac{\delta n_j}{n_{j0}} \right), \tag{9}$$

where the electron and ion response functions, $\mathbf{G}_{e,j}$ (Dimant and Oppenheim 2011, Appendix A), are given by their parallel (i.e., along $\mathbf{B}$),

$$\mathbf{G}_{e\parallel} = \frac{i\kappa_e \mathbf{k}_\parallel}{B}, \qquad \mathbf{G}_{j\parallel} = -\frac{i\tilde{\kappa}_j \mathbf{k}_\parallel}{B}, \tag{10}$$

and perpendicular components,

$$\mathbf{G}_{e\perp} = \frac{i(\mathbf{k}_\perp - \kappa_e(\mathbf{k}_\perp \times \mathbf{b}))}{B\kappa_e}, \qquad \mathbf{G}_{j\perp} = -\frac{i\tilde{\kappa}_j(\mathbf{k}_\perp + \tilde{\kappa}_j(\mathbf{k}_\perp \times \mathbf{b}))}{B(1+\tilde{\kappa}_j^2)}. \tag{11}$$

Here $\mathbf{k}_{\parallel,\perp}$ are the corresponding components of the wave vector $\mathbf{k}$, and

$$\tilde{\kappa}_j \equiv \frac{\kappa_j}{1 - i\omega_{kj}/\nu_j} \tag{12}$$

$$\omega_{ks} \equiv \omega - \mathbf{k} \cdot \mathbf{u}_{s0}. \tag{13}$$

Linearization of the continuity equations yields

$$\omega_{ke} \frac{\delta n_e}{n_{e0}} = \mathbf{k} \cdot \delta \mathbf{u}_e, \qquad \omega_{kj} \frac{\delta n_j}{n_{j0}} = \mathbf{k} \cdot \delta \mathbf{u}_j. \tag{14}$$

Equations for the wave perturbations involve the mean flow velocities, $\mathbf{u}_{s0}$, only through the parameter $\tilde{\kappa}_j$ and Equation (14), i.e., only through the Doppler-shifted wave frequencies ω_{ks}.

Substituting $\delta \mathbf{u}_{e,j}$ from Equation (9) into Equation (14) and invoking the quasi-neutrality condition, $\delta n_e = \sum_j \delta n_j$, we obtain a system of two linear equations for the two unknowns, δn_e and $\delta\Phi$. The existence of a non-trivial solution of this homogeneous system of equations yields the dispersion relation for $\omega(\mathbf{k})$. Skipping the algebra, we present the final result:

$$1 + \sum_j \frac{\omega_{pj}^2 \tilde{\xi}_j [i\omega_{ke}\nu_e\kappa_e^2 - k_\perp^2 u_{te}^2 \xi_e]}{\omega_{pe}^2 \xi_e [\omega_{kj}(\omega_{kj} + i\nu_j)(1+\tilde{\kappa}_j^2) - k_\perp^2 u_{tj}^2 \tilde{\xi}_j]} = 0 \tag{15}$$

where $\omega_{ps}^2 = n_s e^2/m_s\epsilon_0$ is the plasma frequency, $u_{ts}^2 = T_s/m_s$ is the thermal velocity, and

$$\xi_e = 1 + \kappa_e^2 \frac{k_\parallel^2}{k_\perp^2}, \qquad \tilde{\xi}_j = 1 + (1+\tilde{\kappa}_j^2)\frac{k_\parallel^2}{k_\perp^2}. \tag{16}$$

Equation (15) is exact, but to make it tractable analytically we need approximations based on justified assumptions.

3.2. *Growth Rate*

A natural assumption is restricting ourselves to the long-wavelength limit of $|\omega| \sim ku_0 \sim ku_t \ll \nu$ for all species. Firstly, the ion fluid model is strictly applicable only in this limit, because otherwise one would need a more complicated kinetic model for the ion description. Secondly, the long wavelength limit usually provides the minimum threshold field for the FBI. This limit automatically makes all terms $\propto k_\perp^2$ small compared to ω_{ks} and makes the instability growth/damping rate, γ, small compared to the real part of the wave frequency, ω_r. It also allows one to approximate $\tilde{\kappa}_j$ in Equation (12) as $\tilde{\kappa}_j \approx \kappa_j(1 + i\omega_{kj}/\nu_j)$. Note that it is imperative to retain first-order small terms proportional to i because these terms will determine the instability growth rate and threshold field.

Furthermore, even allowing for significant ion magnetization, $\kappa_j \gtrsim 1$, we assume that $(1 + \tilde{\kappa}_j^2)k_\parallel^2/k_\perp^2 \ll 1$. The corresponding small terms are not proportional to i so we will neglect them completely. After applying these two approximations to the relevant accuracy and introducing the more traditional parameter

$$\psi_j = \frac{1}{\kappa_e \kappa_j}\left(1 + \kappa_e^2 \frac{k_\parallel^2}{k_\perp^2}\right), \tag{17}$$

we reduce the dispersion relation given by Equation (15) to

$$1 + \sum_j \rho_j \frac{\omega_{ke}}{\omega_{kj}}\left\{1 + \frac{i}{\omega_{kj}\nu_j}\left[\frac{(1-\kappa_j^2)\omega_{kj}^2 - k_\perp^2 v_{Tj}^2}{(1+\kappa_j^2)} + \frac{T_e}{T_j}\, k_\perp^2 v_{Tj}^2 \psi_j\right]\right\} = 0, \tag{18}$$

where the imaginary terms in the curly bracket are small relative to unity and

$$\rho_j \equiv \frac{n_{j0}}{n_{e0}\psi_j(1+\kappa_j^2)}. \tag{19}$$

In all $\omega_{ks} = \omega - \mathbf{k}\cdot\mathbf{u}_{s0}$, the growth/damping rate is small compared to the corresponding real part, $\omega_{ks}^r = \omega_r - \mathbf{k}\cdot\mathbf{u}_{s0}$.

Retaining first the highest-order real terms in Equation (18) leads to the wave phase-velocity relation for $\omega_r(\mathbf{k})$:

$$1 + \sum_j \rho_j \frac{\omega_{ke}^r}{\omega_{kj}^r} = 0. \tag{20}$$

In the general case of arbitrary ion magnetization, Equation (20) reduces to a polynomial equation for ω_r, whose degree equals the total number of the ion species. For multi-species ions, this equation becomes either unsolvable or its solution is too cumbersome. Below we present a simple approximate solution which applies precisely to chromospheric heights with appreciable ion magnetization. To the next-order accuracy, the imaginary part of Equation (18) yields the growth/damping rate:

$$\gamma = \frac{\sum_j \frac{\rho_j}{\nu_j}\left[\frac{1-\kappa_j^2}{1+\kappa_j^2} - \frac{k_\perp^2 v_{Tj}^2}{(1+\kappa_j^2)(\omega_{kj}^r)^2} + \frac{T_e}{T_j}\frac{k_\perp^2 v_{Tj}^2 \psi_j}{\omega_{ke}^r \omega_{kj}^r}\right]}{\sum_j \frac{\rho_j}{\omega_{kj}^r}\left(\frac{1}{\omega_{kj}^r} - \frac{1}{\omega_{ke}^r}\right)}. \tag{21}$$

The first term in the square brackets describes excitation of the FBI, while the two others describe diffusion losses. Above the magnetization boundary for a given species, $\kappa_j \geq 1$, the corresponding destabilizing term $\propto (1-\kappa_j^2)$ changes its sign and becomes stabilizing (Dimant and Oppenheim 2004).

3.3. *Threshold Electric Field*

The next objective is to calculate the threshold electric field for instability. We examine three cases: no magnetized ions, all magnetized ions, and a single magnetized ion species. The last case best describes the temperature minimum region of the quiet chromosphere. The instability threshold is determined by Equation (21) with $\gamma = 0$, which requires one to solve Equation (20) for the real part of the wave frequency. If some $\mathbf{k}\cdot\mathbf{u}_{j0}$ are not negligibly small then this equation may become a higher-degree polynomial with no explicit solution. Once the threshold electric field, E_{tf}, is known we recover a trigger speed, u_{ts}, with

$$u_{ts} = \frac{E_{tf}}{B} \tag{22}$$

in order to compare to the neutral acoustic speed and the neutral flows that may be responsible for the ambient electric field (Dimant et. al. 2016).

3.3.1. *Unmagnetized Ions*

Madsen et. al. (2014) considered the case where all ions are unmagnetized (and electrons are magnetized). The threshold field under these assumptions is

$$E_{tf}^2 = B^2(1+\psi)^2 \frac{\sum_j \frac{n_{j0}}{\psi_j \nu_j}\left(\frac{m_e \psi_j}{m_j \psi} u_{te}^2 + u_{tj}^2\right)}{\sum_j \frac{n_{j0}}{n_0 \psi_j}} \tag{23}$$

where

$$\psi^{-1} = \sum_j \frac{n_{j0}}{\psi_j \nu_j}. \tag{24}$$

Equation (23) only applies to regions well below the temperature minimum as can be seen in Figure 3.

3.3.2. *Magnetized Ions*

We next consider the case where all ions are magnetized. Fortunately, we may bypass the high-order polynomial mentioned previously due to the following. Introducing the dimensionless parameter

$$\Theta_j \equiv \sqrt{\frac{\kappa_j}{\kappa_e}} = \sqrt{\frac{m_e \nu_e}{m_j \nu_j}}, \tag{25}$$

we verify that it is always small (this can be seen in Figure 3). Assuming strictly perpendicular waves, $k_\parallel = 0$, one can write the parameter ψ_j defined by Equation (17) as $\psi_j = \Theta_j^2/\kappa_j^2$. Due to $\Theta_j \ll 1$, as soon as the ion magnetization becomes noticeable, $\kappa_j \gtrsim 1$, we automatically have $\psi_j \ll 1$. In the E-region ionosphere at altitudes where $\psi_j = \psi \ll 1$, we have $\omega_r = \mathbf{k}\cdot\mathbf{u}_0/(1+\psi)$, so that $|\omega_r - \mathbf{k}\cdot\mathbf{u}_0| \approx \psi|\mathbf{k}\cdot\mathbf{u}_0| \ll |\mathbf{k}\cdot\mathbf{u}_0|$. Expecting a similar inequality to hold for the multi-species Solar chromosphere, we can easily solve Equation (20).

Introducing the relative drift velocity, $\mathbf{v}_{j0} = \mathbf{u}_{e0} - \mathbf{u}_{j0}$, we can express the ion Doppler-shifted frequencies, ω_{kj}, in terms of the corresponding electron frequency as $\omega_{kj} = \omega_{ke} + \mathbf{k}\cdot\mathbf{v}_{j0}$. Assuming by analogy with the E-region $|\omega_{ke}^r| \ll |\mathbf{k}\cdot\mathbf{v}_{j0}|$, we obtain for ω_{kj}^r a simple solution:

$$\omega_{kj}^r \approx \mathbf{k}\cdot\mathbf{v}_{j0}. \tag{26}$$

Inserting this solution to Equation (20), we obtain the corresponding solution for ω_{ke}^r:

$$\omega_{ke}^r \approx -\left[\sum_j \frac{\rho_j}{\mathbf{k}\cdot\mathbf{v}_{j0}}\right]^{-1}. \tag{27}$$

This solution allows us to obtain $\omega_{kj}^r = \omega_{ke}^r + \mathbf{k}\cdot\mathbf{v}_{j0}$ to a better accuracy than zero-order Equation (26). We obtain at the instability threshold

$$E_{\rm tf}^2 = \frac{B^2 \sum_j \frac{\rho_j u_{tj}^2}{\nu_j}\left[\frac{1}{(1+\kappa_j^2)q_j^2} + \frac{T_e}{T_j}\frac{\psi_j}{q_j}\sum_l \frac{\rho_l}{q_l}\right]}{\sum_j \frac{\rho_j(1-\kappa_j^2)}{\nu_j(1+\kappa_j^2)}} \tag{28}$$

In Equation (28) we introduced an angular efficiency parameter

$$q_j \equiv \frac{\mathbf{k}\cdot\mathbf{v}_{j0}}{kE/B} = \frac{\cos\phi - \kappa_j \sin\phi}{1+\kappa_j^2}, \tag{29}$$

where ϕ is the flow angle, i.e. the angle between the wave vector $\mathbf{k}$ and the $\mathbf{E}_0 \times \mathbf{B}$ drift velocity.

3.3.3. *Magnetized Protons & Unmagnetized Heavy Ions*

Assuming that only protons are magnetized and heavy ions (i.e. C^+, Mg^+, Si^+, and Fe^+) are unmagnetized leads to a quadratic equation with an explicit solution. For $j = 1$, corresponding to protons, the general relation for $\omega_{k1}^r \approx \omega_r - \mathbf{k}\cdot\mathbf{u}_{10} = \omega_{ke}^r + \mathbf{k}\cdot\mathbf{v}_{10}$. For all other ions $\omega_{kj}^r \approx \omega_r = \omega_{ke}^r + \mathbf{k}\cdot\mathbf{u}_{e0}$. Defining

$$A \equiv (1+\rho_1)(\mathbf{k}\cdot\mathbf{u}_{e0}) + \left(1 + \sum_{j\neq 1}\rho_j\right)(\mathbf{k}\cdot\mathbf{v}_{10}) \tag{30}$$

and

$$D \equiv A^2 - 4\left(1 + \sum_j \rho_j\right)(\mathbf{k}\cdot\mathbf{v}_{10})(\mathbf{k}\cdot\mathbf{u}_{e0}), \tag{31}$$

we find

$$\omega_{ke}^r = \frac{-A + \sqrt{D}}{2(1+\sum_j \rho_j)} = -d_0 k \frac{E}{B} \tag{32}$$

where

$$d_0 \equiv \frac{1}{2(1+\sum_j \rho_j)}\left\{\cos\phi(1+\rho_1) + \tilde{q}_1\left(1 + \sum_{j\neq 1}\rho_j\right)\right.$$
$$\left. - \sqrt{\left[\cos\phi(1+\rho_1) + \tilde{q}_1\left(\frac{1+\sum_{j\neq 1}\rho_j}{1+\kappa_1^2}\right)\right]^2 - 4\tilde{q}_1\cos\phi\left(1+\sum_j \rho_j\right)}\right\} \tag{33}$$

and the angular efficiency parameter including a new angle allowing for $k_\parallel \neq 0$ is

$$\tilde{q}_1 \equiv \frac{\cos\phi - \kappa_1 \sin\phi\cos\theta}{1+\kappa_1^2}. \tag{34}$$

In Equation (34), we have introduced an orthonormal basis specified by $\langle \mathbf{e},\ \mathbf{b},\ \mathbf{e}\times\mathbf{b}\rangle$, where $\mathbf{e} = \mathbf{E}_0/E_0$, and accompanying spherical coordinate angles $\phi = \arccos(\frac{\mathbf{k}\cdot\mathbf{e}\times\mathbf{b}}{k})$ and $\theta = \arctan(\frac{\mathbf{k}\cdot\mathbf{b}}{\mathbf{k}\cdot\mathbf{e}})$. Substituting back into Equation (21) leads to the threshold electric field:

$$E_{tf}^2 = \frac{B^2 \sum_j \frac{\rho_j u_{tj}^2}{\nu_j}\left[\frac{1}{(1+\kappa_j^2)d_j^2} + \frac{T_e}{T_j}\frac{\psi_j}{d_j d_0}\right]}{\sum_j \frac{\rho_j(1-\kappa_j^2)}{\nu_j(1+\kappa_j^2)}}, \tag{35}$$

where

$$d_j = -d_0 + \delta_{1j}\cos\phi + (1-\delta_{1j})\tilde{q}_1 \tag{36}$$

and δ_{ij} is the Kronecker delta. Again, Equation (35) is the analytic solution appropriate for the temperature minimum region of the chromosphere. We include the asymptotic solutions given by Equations (23) and (28) for completeness.

4. NUMERICAL SOLUTION FOR THE THRESHOLD FIELD

Thus far we have worked analytically, but it is prudent to include a numerical approach as a check and for cases which violate the assumptions inherent in Equation (35). The first task is to find a robust method to solve $D(\omega, \mathbf{k}) = 0$. Given a wave vector $\mathbf{k}$, we find ω using a nonlinear root-finding algorithm with the full dispersion relation, Equation (15). Specifically, we use Muller's method (Muller 1956; Press et al. 2007) since it functions well in the complex plane. Muller's method is a type of secant method that constructs a parabola using three points and chooses the intersection of that parabola and the zero plane as a new point for the next iteration. Because this process involves the quadratic formula, a real seed can produce a complex root. This allows ω to have an imaginary component, the growth/damping rate, while $\mathbf{k}$ is purely real.

The seed is the solution to the dispersion relation that does not include magnetized ions. We choose a drift velocity given by the trigger velocity with unmagnetized ions (Madsen et. al. 2014). The trigger velocity is the electron drift velocity at which the growth rate is zero (i.e. the onset of instability). Choosing the trigger velocity as the input drift velocity allows the seed ω value to be purely real. In regions of parameter space where the solution with and without magnetized ions is significantly different, we begin in a region in which this is not the case and slowly move to the original region of interest, using each solution as the seed for the next. The orientation and magnitude of the background fields and wave vector are arbitrary and the configuration can be chosen.

With these input and seed parameters, we have a robust method for calculating $\omega = \omega_r + i\gamma$. To find the threshold field, another non-linear root-finding algorithm is applied to find the ω at which $\gamma = 0$, where the electric field is the varying parameter and the magnetic field is fixed. Each iteration of this second algorithm requires the solution to the dispersion relation. To summarize, we solve $\gamma(E) = 0$ for E, where each iteration requires the solution to $D(\omega) = 0$ for ω. The magnetic field, wave vector, and orientation of $\mathbf{E}$ are specified and arbitrary.

5. INSTABILITY IN THE CHROMOSPHERE

We begin by calculating the threshold field and trigger speed using the three analytic expressions in Section 3.3 as well as the numerical method in Section 4 using the parameters for the chromosphere obtained from the model in Section 2. Figure 5 compares the trigger speeds (Equation (22)) corresponding to these threshold fields for a magnetic field of 50 G. "Unmagnetized ions" refers to the expression from Section 3.3.1, "magnetized ions" to the expression from Section 3.3.2, and "magnetized protons" to the expression from Section 3.3.3. Clearly the case assuming magnetized protons and unmagnetized heavy ions matches best with the numerical result that used the full dispersion relation, Equation (15). This is not surprising given that the temperature minimum region of the chromosphere satisfies these assumptions for typical quiet-chromosphere magnetic fields.

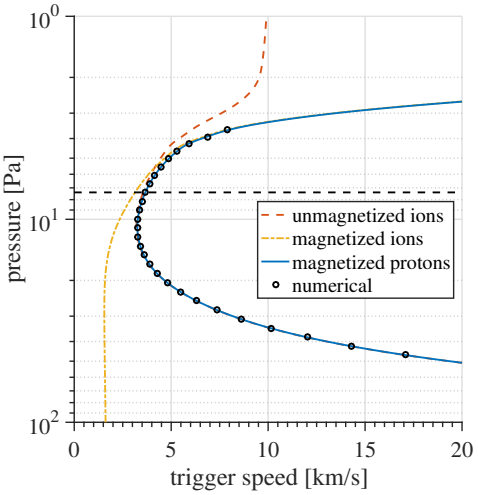

Figure 5. A comparison of the three analytic expressions and the numerical result for the trigger speed. The magnetic field is 50 G. It is clear the numerical result agrees best with the expression derived assuming magnetized electrons, magnetized protons, and unmagnetized heavy ions (Equation (35)). The horizontal dash line marks the temperature minimum.

Figure 6 shows the effect of varying the ambient magnetic field. There is a cutoff introduced by the inclusion of magnetized protons. Above a certain altitude, the protons short out the instability. Mathematically, this is seen as the denominator of Equation (35) approaching zero as κ_1 increases. Also note that the heavy ions have a destabilizing effect even for κ_1 slightly larger than unity. This is true despite ignoring Coulomb collisions and thermal instabilities, both of which are destabilizing (Gogoberidze et. al. 2009, 2014).

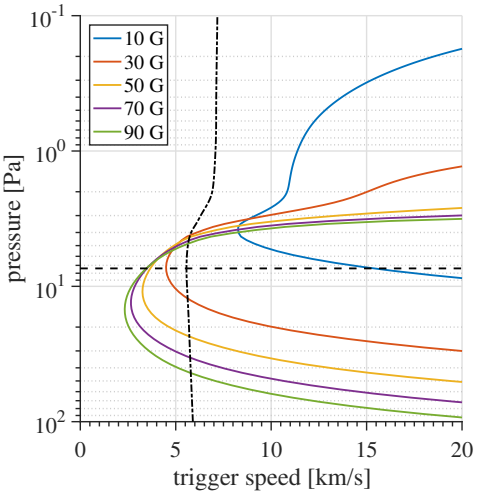

Figure 6. The trigger speed as a function of pressure and magnetic field. The lines are theoretical solutions (Equation (35)). The dash-dot line is the neutral acoustic speed and the horizontal dash line marks the temperature minimum.

As the magnetic field increases, the altitude at which the minimum trigger speed is located decreases. However, the minimum trigger speed is always near the heating region for these parameters. The neutral acoustic speed is included as a point of comparison. For fields greater than 20 G, the trigger velocity (corresponding to the threshold field divided by B) falls below the acoustic speed; this does not occur even in the ionosphere where electrojets are known to form.

One dimensional models are useful, but the chromosphere is dynamic, time-dependent, and out of equilibrium. The effect on ion magnetization is seen more clearly in Figures 7 and 8, which show the ratio of electric field to the threshold electric field with and without ion magnetization included respectively. **The electric field in these figures comes from 2.5-dimensional simulations detailed by Martínez-Sykora et. al. (2017) using the code Bifrost (described by Gudiksen et. al. (2011)).** Figures 7 and 8 show a snapshot of radiation magnetohydrodynamic (MHD) simulations of the chromosphere. **Unlike previous figures, the vertical axis on Figures 7 and 8 is a height scale instead of pressure scale. The reason is that the pressure in the simulation is not monotonic in z and varies with time and space, and therefore there is no longer a one-to-one mapping between height and pressure.** The induced electric field is $-\mathbf{u}_n \times \mathbf{B}$, where $\mathbf{u}_n$ is the bulk velocity. Ion species fractions are estimated as a function of pressure using from the model described in Section 2. Figures 7 and 8 indicate that the neutral wind induced field by itself may drive the FBI in certain regions of the chromosphere. These regions are also where heating occurs.

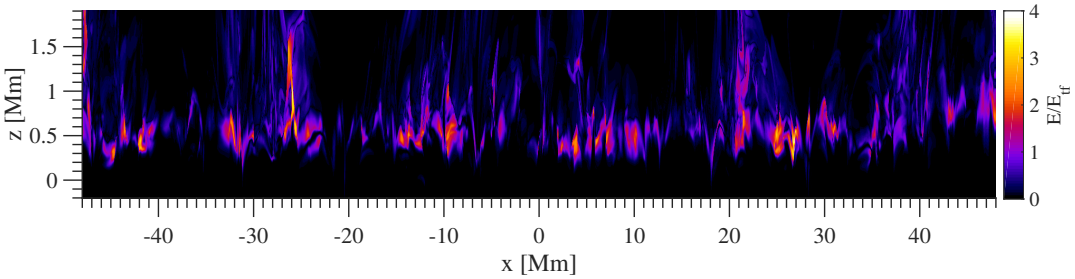

Figure 7. The ratio of electric field in MHD simulations (Martínez-Sykora et. al. 2017) to the threshold electric field given by Equation 35, which includes the effect of ion magnetization.

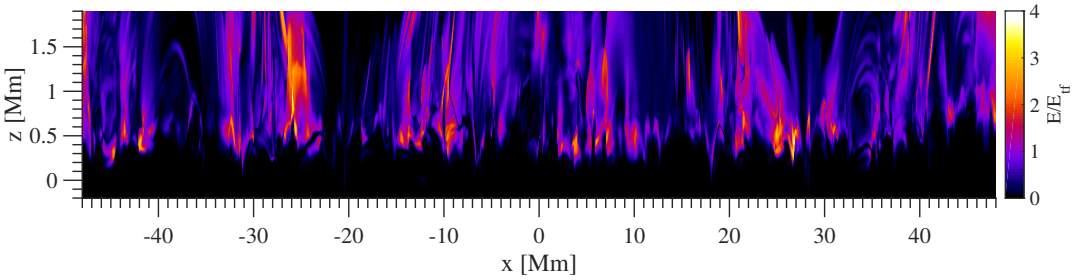

Figure 8. The ratio of electric field in MHD simulations (Martínez-Sykora et. al. 2017) to a threshold electric field that does *not* include the effect of ions or ion magnetization.

If exceeding the drift speed was the only criterion for the FBI, electrojets would not exist on Earth. There are multiple ways the drift velocity can be enhanced which would not be evident from estimating the drift velocity from the observed current. Enhancements in both the equatorial and auroral ionosphere drive the drift speed far above the trigger velocity. In the equatorial region on Earth, the enhancement is due not only to the neutral wind induced drift, but also changing conductivity layers as a function of height. This is the criteria for electrojet formation laid out in Dimant et. al. (2016). We also expect that electrojet-like enhancements such as described in Dimant et. al. (2016) would increase the FBI drivers further as they do in the Earth's ionosphere.

We argue that electron heating by the FBI may be highly consequential. Gogoberidze et. al. (2009) did not take into account the effect of additional electron heating related to the presence of parallel electric field in waves. As shown theoretically by Dimant and Milikh (2003) and confirmed by recent particle-in-cell simulations (Oppenheim and Dimant 2013), this effect can significantly increase the electron heating. This mechanism elevates electron temperatures in the auroral ionosphere by as much as one order of magnitude. The importance of this mechanism for the solar

chromosphere requires separate analysis and is out of the scope of this paper.

Since the FBI may be responsible for electron heating, it is also interesting to examine how the FBI changes as the ratio T_e/T_i increases. Figure 9 shows the instability threshold increases along with the temperature ratio. This is expected as it means that the saturation of the instability is stabilizing. If this were not the case, the instability would be explosive. It is also of significance to the nonlinear phase of the FBI (Dimant and Milikh 2003), where the turbulence intensity is affected by the temperature ratio.

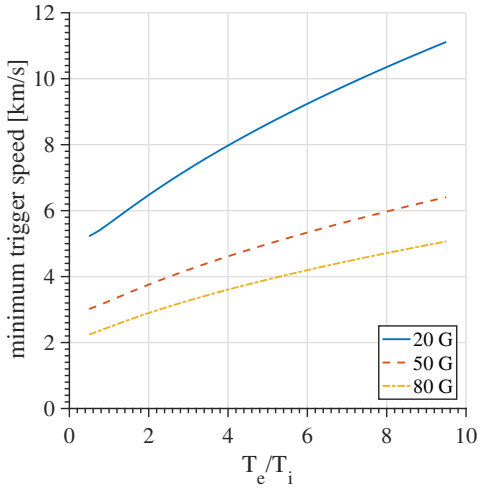

Figure 9. The effect of varying the temperature ratio on the minimum trigger speed. This is meant to simulate the effect of electron heating on the instability.

In the simpler theory of the FBI, the orientation of $\mathbf{k}$ corresponding to the maximum growth is parallel to $\mathbf{E}_0 \times \mathbf{B}$. In our case, the drifts (given by Equation (5)) are no longer strictly in the $\mathbf{E}_0 \times \mathbf{B}$ direction, so we expect the optimal angle might also vary. Figure 10 shows how the trigger speed changes as these angles vary. For even small values of θ, the optimal direction of $\mathbf{k}$ is still along $\mathbf{E}_0 \times \mathbf{B}$. However, it is interesting to note that the global minimum of the minimum trigger speed occurs at $\theta = 0^o$ ($k_\parallel = 0$) and $\phi \approx -8^o$, i.e. not along $\mathbf{E}_0 \times \mathbf{B}$.

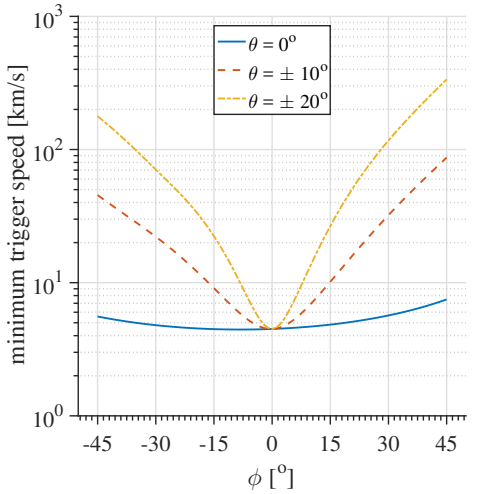

Figure 10. The minimum trigger speed as a function of the orientation of the wave vector $\mathbf{k}$ for the 50 G case. The minimum of the solid blue curve is at $\phi \approx -8^o$.

6. CONCLUDING REMARKS

This paper introduces ion magnetization to the analysis of the FBI in the solar chromosphere. Numerically solving a new dispersion relation and combining it with a model of the chromosphere allows us to characterize the threshold

electric fields and corresponding trigger speeds. We find that, depending on magnetic field strength, the minimum trigger speed is produced near the temperature minimum. We also find an asymptote that limits the instability to a certain region due to the protons shorting it out, an effect not seen in previous theories. The source of the electric field that is responsible for the drifts will be the subject of a future paper. The threshold fields and trigger speeds calculated in this work can serve as a point of comparison to determine how likely it is that the FBI contributes to heating in the chromosphere.

This work was supported by NSF-AGS Postdoctoral Research Fellowship Award No. 1433536 and NSF/DOE Grant No. PHY-1500439. The authors also acknowledge a recent contribution from William Longley.

REFERENCES

Athay, R. G. 1966, ApJ, 146, 223
Buneman, O. 1963, PhRvL, 10, 285
Bahcivan, H. 2007, Geophys. Res. Lett., 34, L15106, doi:10.1029/2006GL029236.
Campos, L. M. B. C., & Mendes, P. M. V. M. 1995, MNRAS, 276, 1041
Carlsson, M., & Stein, R. F. 1992, ApJ, 397L, 59
Carlsson, M. 2007 ASPC, 368, 49
Dalgarno, A., McDowell, M. R. C., & Williams, A. 1958, RSPTA, 250, 411
Dimant, Y. S. and Milikh, G. M. 2003, J. Geophys. Res., 108, 1350, doi:10.1029/2002JA009524
Dimant, Y. S., Oppenheim, M., M. 2004, J. Atmos. Terr. Phys., 66, 1639-1654
Dimant, Y. S., Oppenheim, M. M. 2011, J. Geophys. Res., 116, A9
Dimant, Y. S., Oppenheim, M. M., Fletcher, A. 2016, Phys. Plasmas, 23, 084503
Farley, D. T. Jr. 1963, J. Geophys. Res., 68, 6083
Freytag, B., Steffen, M., Ludwig, H.-G,. Wedemeyer-Bhm, S., Schaffenberger, W., & Steiner, O. 2012, CoPh, 231, 919
Fontenla, J. M., Avrett, E. H., & Loeser, R. 1991, ApJ, 377, 712
Fontenla, J. M., Avrett, E. H., & Loeser, R. 1993, ApJ, 406, 319
Fontenla, J. M., 2005, A&A, 422, 1099F
Fontenla, J., Curdt, W., Avrett, E. H., & Harder, J. 2007, A&A, 468, 695
Fontenla, J. M., Peterson, W. K., & HArder, J. 2008, A&A, 480, 839F
Fontenla, J. M., Curdt, W., Haberreiter, M., Harder, J., & Tian, H. 2009, ApJ, 707, 482
Foster, J. C., & Erickson, P. J. 2000, GeoRL, 27, 3177
Gogoberidze, G., Voitenko, Y., Poedts, S., and Goossens, M. 2009, ApJL, 706, 12L
Gogoberidze, G., Voitenko, Y., Poedts, S., & De Keyser, J. 2014, MNRAS, 438, 3568-3576
Gudiksen, B.V., Carlsson, M., Hansteen, V.H., Hayek, W., Leenarts, J., Martnez-Sikora, J. 2011, A&A, 531, A154
Liperovsky, V. A., Meister, C. -V., Liperovskaya, E. V., Popov, K. V., and Senchenkov, S. A. 2000, Astronomische Nachrichten, 321, 2
Madsen, C. A., Dimant, Y. S., Oppenheim, M. M., and Fontenla, J., M. 2014, ApJ, 783, 128
Martínez-Sykora, J., De Pontieu, B., Hansteen, V. H., Rouppe van der Voort, L., Carlsson, M., and Pereira, T. M. D. 2017, Science, 356, 6344, 1269-1272
Muller, D. E., 1956, Mathematical Tables and Other Aids to Computation, 10, 56
Nordlund, A., Spruit, H. C., Ludwig, H.-G., & Trampedach, R. 1997 A&A, 328, 229
Oppenheim, M. M. & Dimant, Y. S., 2013, J. Geophys. Res., 118, 1306-1318
Press, W. H., Teukolsky, S. A., Vetterling, W. T., Flannery, B. P., 2007. Numerical Recipes: The Art of Scientific Computing (3rd ed.). (New York, Cambridge University Press)
Rieutord, M., Roudier, T., Rincon, F., Malherbe, J.-M., Meunier, N., Berger, T., & Frank, Z. 2010, A&A, 512A, 4
Schunk, R., & Nagy, A. 2009, Ionospheres, (2nd ed.; New York, NY: Cambridge University Press)
Sudan, R. N., Akinrimisi, J., and Farley, D. T. 1973 J. Geophys. Res., 78, 240
Vögler, A., Shelyag, S., Schssler, M., Cattaneo, F., Emonet, T., & Linde, T. 2005, A&A, 429, 335